Two- and Four-Electrode Configurations for Contactless Reinforced Concrete Corrosion Monitoring

B. Díaz, X.R. Nóvoa, C. Pérez, A. Pintos, Vincent Vivier

Two and four-electrode configurations for contactless reinforced concrete corrosion monitoring

B. Díaz,* X.R. Nóvoa,‡,* C. Pérez,* A. Pintos,* V. Vivier**

‡Corresponding author. E-mail: rnovoa@uvigo.es.

*CINTECX, Universidade de Vigo, EEI, ENCOMAT Group, 36310 Vigo, Spain.

**Sorbonne Université, CNRS, Laboratoire de Réactivité de Surface, Paris, France

ABSTRACT

The paper addresses the need for a fast and reliable method for field monitoring of reinforced concrete structures. A proof of concept is presented where a non-contact procedure provides quantitative information on the concrete resistivity and reinforcement corrosion rate. A Wenner-type probe is presented, where a combination of two and four-electrode measurements in a relatively high-frequency domain allows obtaining the information of interest. The method is based on the fact, verified by numerical simulations, that the embedded rebar works as an effective floating counter electrode and thus, for distances higher than a critical value (1 cm in the simulations done), the ratio of concrete resistivity to the measured impedance at 1 kHz is constant and only dependent on the electrode diameter. The apparent polarization resistance measured with the four-electrode arrangement and normalized to the concrete resistivity allows obtaining the actual polarization resistance without contacting the rebar whose distance to the electrodes shall be known.

KEY WORDS: *Contact-less method, corrosion rate determination, impedance spectroscopy, steel in concrete.*

1 INTRODUCTION

Reinforced concrete is one of the most used materials for civil and industrial structures. When properly designed, according to the environment aggressiveness, the material is durable because the concrete cover provides a protective barrier against rebar corrosion. However, as the design life approaches or unforeseen events may cause premature failure, periodical inspection of the structures is mandatory to plan repairs and prevent unexpected failures. Predicting the remaining service life of structures requires [1] data from non-destructive testing (NDT), and among NDT, the electrical methods allow to estimate the corrosion state or the corrosion rate. As described in a recent extensive review[2], the electrical methods require an electronic device with two, three, or four electrodes to determine the relevant parameters: the corrosion potential, the corrosion rate (via polarization resistance (*Rp*), Tafel scan or galvanostatic pulse), and the concrete resistivity. For the concrete resistivity measurements using the Wenner method[3], no direct contact with the rebar is required[2]; however, for the other techniques, electrical contact with the specific rebar is required, which cannot always be achieved. In addition, the associated experimental procedures described on standards as the ASTM C876 standard[4] or the RILEM recommendations[5] for potential mapping are time-consuming and not well adapted to field application, especially for hard-to-reach places.

The continuous struggle for finding new and effective methods that avoid the need for electrical contact with the rebar to be inspected has led to the development of magnetic NDT as the recently published[6] based on pulsed eddy currents. However, the information retrieved remains qualitative because only rebars with a certain amount of corrosion products can be detected, as it occurs for ground-penetrating radar[7].

Thus, gathering quantitative information about the current corrosion rate still requires an electrochemical method that involves Faraday's law of equivalence between mass lost and charge passed. The critical question is how to measure a faradaic current without contacting the rebar.

The possibility of measuring the corrosion rate of an embedded element has been explored in several attempts, although with limited practical success[8–12]. Some years ago, the concept of the floating electrode was introduced to study buried conducting materials[13] and applied to different situations[14]. However, using that idea requires previous knowledge of the ionic resistivity of the conducting medium and the distance between the measuring electrodes and the rebar. Although magnetic procedures can easily estimate the electrode-rebar distance, the determination of the resistivity is more intricate because the Wenner probe requires the electric field injected into the system to be free of the influence of underlying reinforcing bars.

The challenge we address in the present communication is how the Wenner probe can be used for both concrete resistivity and corrosion rate determinations in a single measurement. The resistivity, determined in the local area under test, will be used for normalization of the resistance measured (depending on the behavior of the floating electrode) but will also serve as a double check on the corrosion rate estimation due to the close relationship between both values[15].

Numerical simulations performed in the floating electrode study[13] showed that the Wenner probe used in AC mode (four-point impedance measurements) generates no current distribution in the high-frequency domain. This fact can be coupled with the resistance (R) of a disk electrode of radius r_0 in an insulating medium of resistivity ρ, provided the counter electrode is far enough[16,17]. The relationship for a disk electrode between the measured resistance R, and the resistivity ρ, according to Eq. 1, can give the key to the single-step measurement we are searching for.

$$\rho = R \cdot 4r_0 \tag{1}$$

The present communication presents evidence that a combination of two and four-electrode measurements allows proper corrosion rate determinations in a single and fast step, reproducing the three-electrode measurement values taken as the reference.

2 EXPERIMENTAL PROCEDURES

Three nominally identical prismatic pieces of 4 x 4 x 16 cm^3 were prepared using cement paste (CEM I 52.5R), with a 0.5 water/cement ratio. 1/3 of the prism length (so, 4 x 4 cm^2) was dedicated to the measurement of the resistivity in a classical 2-electrode arrangement using two graphite sheets, as depicted in Fig. 1. The remaining 2/3 of the prism was dedicated to performing corrosion rate determinations on an embedded wire (ϕ = 0.1 cm, L = 8.3 to 8.8 cm). Reference corrosion rate determinations were performed using a classical 3-electrode arrangement with an external graphite counter electrode and a saturated calomel electrode as reference. Prospective corrosion rate measurements were performed with 2- and 4-electrode measurements using the Wenner-type probe depicted in Fig. 1. A drop of conducting gel defining a contact surface nominally equal to that of the probe's tip was employed to guarantee good ionic contact. Thus, the classical 3-electrode measurements were used as the reference to validate the 4-electrode Wenner-type measurements. The position of the wire under test was varied so that its distance to the Wenner probe was 1, 2, and 3 cm, which corresponds to different cover thicknesses as shown in Fig. 1.

Moreover, additional pieces were prepared to determine the validity of the proposed methodology in the active corrosion state. Thus, pastes with the addition of chloride ions (as NaCl) were fabricated, one containing 1.2% and the other 2.4% of chlorides (cement weight percent). The embedded wires were subjected to anodic current densities of 2 and 1 mA/cm^2 for 24 hours, respectively. After the polarization, the measurements were started under the damp condition for the first analysis. Additional measurements were also periodically performed after several days of air-drying to gather data with several cement paste resistivity values.

An Autolab® PGSTAT 204 potentiostat was used for the 4- and 2-electrodes measurements in the Wenner-type configuration. The separation between the electrodes (denoted "a" in Fig. 1) was 1 cm, 1.5 cm, or 2 cm. The diameter of the measuring electrodes was 0.28 cm. A homemade device was built for these measurements, where holes at several distances were drilled so that the measuring electrodes could be positioned at the required distances. All the measurements were recorded with the rightmost electrode placed at a distance of 2 cm from the right side of the prism, as shown in Fig. 1. The analyzed frequency range was from 100 kHz to 100 mHz, recording 6 points per decade with an amplitude signal of ±10 mV. For the 2-electrode measurements in this configuration, the connection of the internal electrodes was short-circuited to that of the corresponding external electrodes and maintained the 1 cm, 1.5 cm, and 2 cm distances. The internal electrodes were left disconnected. The low-frequency limit was fixed at 10 Hz in this case.

The PGSTAT 204 potentiostat was also used for the conventional 3-electrodes measurements to determine the actual polarization resistance of the embedded wires. Two external graphite sheets (4 x 8 cm^2 each) placed at both sides of the prism, facing the embedded wire, were used as the auxiliary electrode (a damp sponge allowed ionic conduction), and an SCE placed on top was the reference electrode. Six frequency points per decade were recorded, with 10 mV signal amplitude, in the frequency range from 100 kHz to 10 mHz.

The actual resistivity of the system was determined using the experimental arrangement depicted in Fig. 1 (left). The cell constant for such arrangement is 4 cm (16 cm^2 square shape electrodes separated by 4 cm). As the electrodes are not guarded, the 25% of the electrode perimeter facing the remaining prism allows some current leakage which will result in resistivity underestimation to a maximum of 7%[18]. The measurements were performed using an Agilent 4294A analyzer. The measurements, 15 data points per decade between 110 MHz and 40 Hz, were recorded with 50 mV signal amplitude.

All the samples were immersed in water (or a saturated NaCl solution for the case of the pieces prepared with the addition of chlorides) before the beginning of the measurements. After the first measurement done under the damp condition, the samples were air dried, and the measurements were periodically performed over several days. The purpose of this experimental plan was the assessment of several measurements with different resistivity values of the cement paste cover.

3 RESULTS

3.1 Resistivity measurement

Table 1 summarizes an example of the evolution of the material's resistivity upon drying. The values were extracted from the EIS measurements as represented in Fig. 2, assuming the percolation model described elsewhere[19,20] and considering the value of 4 cm for the cell constant described above. The resistivity thus corresponds to four times the diameter of the capacitive arc depicted in Fig. 2 as an example. The low-frequency tail corresponds to the beginning of the contribution of the graphite electrodes, and it is not of interest here. As expected, resistivity increases upon drying in the laboratory atmosphere until reaching a maximum of about 13 kΩ cm upon mild oven-drying.

To test the proposed method's validity, impedance measurements were performed using the Wenner-type probe but short-circuiting the internal electrodes to the external ones (thus, a 2-electrode measurement), leaving the internal electrodes disconnected. Fig. 3 corresponds to one example of the type of plot obtained. The value of the real part of the impedance at about 1 kHz was ascribed to the resistance, 2*R*, allowing the resistivity value, ρ, to be calculated with the help of Eq. 1. The measured resistance is double the R-value to be entered in Eq. 1 because the two identical electrodes are placed in series. The remaining low-frequency part of the spectra corresponds to the contributions of the four interfaces forming a RC time-constant due to the capacitance and the faradaic impedance of the electrode, that is the impedance of the electrode used for performing the measurement. It is worth mentioning that the high frequency shift of the impedance towards higher values is due to the increase in resistance of the cement paste during the drying step. Fig. 4 compares the resistivity values obtained using the proposed method and the reference values obtained using the cubic section of the prism depicted in the left side of Fig. 1. Five humidity contents and two distances electrodes-embedded wire were compared. Overall, a good agreement between both types of measurements was obtained. However, the dispersion is higher for the shorter electrodes-wire distance (Fig. 4A for d = 1 cm), which can be understood as the counter electrode (the floating embedded wire) is not far enough from the current-driven electrode. On the other hand, in Fig. 4B (corresponding to d = 3 cm), the distance to the counter electrode seems to be large enough to validate the use of Eq. 1. A particular case is the situation of oven-dried samples for which the calculated resistivity is about twice the actual value and shows higher dispersion. This can be ascribed to the method employed for contacting the current-driven electrodes and the structure, a droplet of conducting gel that tends to shrink through the empty pores and defines an actual diameter smaller than the geometrical one.

3.2 Polarization resistance measurements: apparent and actual

On each batch of measurements, besides the resistivity measurements described in the previous section, impedance measurements using the classical 3-electrode arrangement and the Wenner-type probe (4-point measurement) were performed, providing the actual value of R_p (R_p^0, in Ω.cm^2), and the apparent Rp (*Rp*, in Ω), respectively. For this purpose, the potential of the steel was studied for two different conditions: a passive state and a potential in the active dissolution domain as shown in Figs. 5 and 6, respectively. For the passive state, the value of the real part of the impedance at 10 mHz was taken as R_p^0 because it is very close to the one found appropriate to match the mass loss data[21,22]. It has been shown[22] that the charge transfer resistance in the passive state can be accessed in the 1-10 mHz window, which corresponds with the suitable sweep rate in Rp technique that makes matching the electrochemical and gravimetric data[21]. For the active condition, the diameter of the capacitive impedance loop was taken as R_p^0.

Whatever the condition of the rebar, passive or active, the impedance spectra obtained using the 4-electrode Wenner-type probe had a similar shape to that shown in Fig. 7, which can be understood owing to the parallel contribution of the cement paste in the low-frequency range. Roughly the spectra rotate left in frequency as the cover thickness increases, e.g., in Fig. 7, the impedance at 1 kHz shows capacitive, resistive, and inductive features as the cover thickness increases from 1 cm to 3 cm, respectively. Moreover, the capacitive loop decreases diameter, as described for a floating electrode[13], where a relationship was established between the diameter of the capacitive loop and the actual polarization resistance, for a specific probe's geometry and cover thickness. The limit situation is a cover thickness where the current cannot reach the embedded bar, so that the capacitive feature vanishes.

The relationship between the diameter of the capacitive loop obtained using the 4-electrode Wenner-type probe, R_p, and the actual polarization resistance, R_p^0, obtained from the 3-electrode measurement was verified in this research. After normalization of both values by the cement paste resistivity (obtained by the 2-electrode Wenner method described above), plots as those presented in Fig. 8 were obtained. The

linear relationship is clear, no matter the resistivity of the sample. Interestingly, the plot slope increases with the distance "a" between the sensing electrodes, representing increased sensitivity of the 4-electrode measurement.

3.3 Numerical simulations

To validate the confidence and the explanation of the experimental measurements presented in the previous section, a series of numerical simulations in a 3D model reproducing the geometry of the experimental probes was conducted by finite element methods. 2- and 4-electrode simulations with different parameter values for a, d, ρ, and R_p and C_{dl} were computed assuming that:

a) Inside the concrete, the potential distribution is governed by the Laplace's equation, which expresses in Cartesian coordinates as Eq. 2:

$$\frac{\partial^2 V}{\partial x^2} + \frac{\partial^2 V}{\partial xy^2} + \frac{\partial^2 V}{\partial z^2} = 0 \tag{2}$$

Where V is the potential.

b) The electric insulation condition on each surface of the concrete is expressed as Eq. 3:

$$\frac{\partial V}{\partial n} = 0 \tag{3}$$

where n is the normal direction to the concrete surface.

c) The flux boundary condition at the rebar/concrete interface is given by Eq. 4:

$$-\kappa \frac{\partial \tilde{V}}{\partial n} = \left(j\omega C_0 + \frac{1}{R_p}\right)\left(\tilde{V} - \tilde{V}_0\right) \tag{4}$$

where C_0 is the interfacial capacitance, R_p the polarization resistance, ω the angular frequency, κ the concrete conductivity $\left(\kappa = \frac{1}{\rho}\right)$, and V_0 the potential of the concrete just outside the double layer.

These equations were solved in the frequency domain, thus allowing the direct calculation of the system's impedance. Only the external electrodes were used for the two-electrode configuration, and a potential condition is applied to both electrodes. The impedance was thus obtained as the ratio of the potential of one of these two electrodes to the current flowing through the same electrode. For the four-electrode configuration, the external electrodes were used to inject locally the current density, and the local potential difference was probed using the two internal electrodes. In that case, the impedance was obtained as the ratio of the current of one internal to the immediate adjacent electrode used to probe the local potential.

Fig. 9a shows that the current lines at 1 kHz focus on the embedded rebar so that if the chosen frequency is higher (> ~5 times) than the characteristic frequency of the rebar's interface, the only resistance found for current flow is the resistance of the cement paste. Thus, the

embedded rebar acts as a floating counter electrode, and then Eq. 1 is applicable (for "d" large enough). For lower frequencies, Fig 9b shows the current also flows through the electrolytic conductor, parallel to the rebar, and enters the rebar via R_p when the signal frequency approaches the characteristic frequency of the interface and goes to DC. The resulting measured response should correspond to that mixed conduction described in detail elsewhere[13].

Sweeping the frequency above and below the characteristic frequency of the rebar's interface, f_c (Eq. 5), it is then possible to obtain the whole spectra of current distributions that, taking the potential at specific sites, allow obtaining the desired impedance spectra. Fig. 10a corresponds to the 2-electrode arrangement, i.e., potential readings at the external electrodes, and Fig 10b to the 4-electrode arrangement, i.e., potential readings at the internal electrodes of the Wenner-type setup.

$$f_c=1/(2\pi R_p C_0) \quad (5)$$

The first interesting feature noted when comparing Fig. 10a to 10b is that the real axis is wholly shifted in the 4-electrode (Fig. 10b) measurement compared to the 2-electrode measurement (Fig. 10a), indicating that the high-frequency limit in the case of Fig. 10b is not related to the resistivity of the cementitious cover. Furthermore, simulations (not shown) varying the cement resistivity did not produce systematic variations in the high-frequency limit. A second interesting feature is the diameter of the capacitive arc, similar in both Fig. 10a and 10b, which can be of interest from a practical point of view because that diameter corresponds to the apparent R_p that can be correlated to the actual R_p, as shown elsewhere[13,14] and in Fig. 8. Moreover, Fig. 10a shows an inductive feature that is not present in Fig. 10b. Such feature was also observed experimentally in some of the EIS spectra presented in Fig. 3. As the model does not include inductive elements, the observed feature should be linked to the cell geometry and associated current distribution. So far, we do not have a clear explanation for this inductive effect observed in the low-frequency limit for the 2-electrode arrangement (experimental and simulations).

The high-frequency limit of the 2-electrode measurement follows systematic variation with the cement resistivity, as Fig. 11 shows. The real part of the impedance at 1 kHz tends to have stable values for distances to the embedded bar greater than 1 cm. Moreover, in that region, as indicated in Fig. 11, the ratio ρ/Z_r = 0.23 cm, no matter the resistivity value. According to Eq. 1, this ratio should only depend on the electrode radius, which is verified here.

4 DISCUSSION

Fig. 4 shows that whatever the distance "a" of the sensor, for the resistivity measurements, the embedded wire acts as the effective (floating) counter electrode thus, the relevant distance to fulfill the condition of applicability of Eq. 1 is the distance to the embedded rebar. This is so because at high frequency (about 1 kHz in the present case), almost 100% of the current goes through the rebar (wire) after crossing the ionic conductor (cement paste), perpendicular to the rebar. A negligible current fraction flows only through the ionic conductor[13] parallel to the rebar. Nevertheless, the ionic contact between the electrodes and the cementitious element becomes critical for dry conditions to maintain the geometry (effective probe diameter). In this context, for a practical application, it seems convenient to perform the measurement on not too dry days or to pre-wet the surface, as recommended in the ASTM C876 standard[4] for corrosion potential determinations.

The numerical simulations show that Eq. 1 holds for the 2-electrode measurement; however, the ratio ρ/Z_r = 0.23 is about $2r_0$ instead of $4r_0$. This fact is because of the 2-electrode measurement that contains twice (anode and cathode) the resistance considered in Eq. 1.

The numerical model contains interfacial resistance and capacitance for the embedded rebar but not for the current-driven electrodes; thus, the diameter of the capacitive arc in Fig. 10a should be increased by the amount of the corresponding interfacial resistance. Obviously, the experimental data in Fig. 3 contain the electrode surface resistivity. That is probably why the low-frequency inductive feature is less marked and only evident for the measurement at six days of drying.

5 CONCLUSIONS

The above presented results on EIS measurements performed on wires embedded in cement paste of different resistivity, using 2, 3, and 4-electrode probes, have allowed deriving the following conclusions:

- A proof of concept was presented, showing the possibility of assessing the corrosion rate (via R_p) and resistivity in a single measurement.
- Numerical simulations show that the current distribution in the system allows the 2-electrode resistivity determination.
- The experimental data show a good relationship between apparent and actual polarization resistances, normalized to the material's resistivity. Furthermore, the sensitivity of the 4-electrode measurement (the slope in Fig. 8) increases with the distance "a" between electrodes.

6 ACKNOWLEDGMENTS

The authors from UVigo acknowledge grant # ED431B2021/14 from Xunta de Galicia Government.

7 REFERENCES

1. Luo, D., Y. Li, J. Li, K.-S. Lim, N.A.M. Nazal, and H. Ahmad, *Sensors* 19 (2018): p. 34, http://www.mdpi.com/1424-8220/19/1/34.
2. Rodrigues, R., S. Gaboreau, J. Gance, I. Ignatiadis, and S. Betelu, *Constr. Build. Mater.* 269 (2021): p. 121240.
3. Miccoli, I., F. Edler, H. Pfnür, and C. Tegenkamp, *J. Phys. Condens. Matter* 27 (2015): p. 223201, http://stacks.iop.org/0953-8984/27/i=22/a=223201?key=crossref.5f146e5ca8d78e9795a89548e891758e.
4. ASTM-International, "ASTM C876-15. Standard Test Method for Corrosion Potentials of Uncoated Reinforcing Steel in Concrete" (2016), https://www.astm.org/c0876-15.html.
5. Elsener, B., C. Andrade, J. Gulikers, R. Polder, and M. Raupach, *Mater. Struct.* 36 (2003): pp. 461–471, https://www.rilem.net/boutique/fiche.php?cat=journal&reference=1218.
6. Tamhane, D., J. Patil, S. Banerjee, and S. Tallur, *IEEE Sens. J.* 21 (2021): pp. 22086–22093, https://ieeexplore.ieee.org/document/9509426/.
7. Hong, S., H. Wiggenhauser, R. Helmerich, B. Dong, P. Dong, and F. Xing, *Corros. Sci.* 114 (2017): pp. 123–132.
8. Zhang, J., P.J.M. Monteiro, and H.F. Morrison, *ACI Mater. J.* 98 (2001): pp. 116–125, http://www.concrete.org/Publications/ACIMaterialsJournal/ACIJournalSearch.aspx?m=details&ID=10195.
9. Zhang, J., P.J.M. Monteiro, and H.F. Morrison, *ACI Mater. J.* 99 (2002): pp. 242–249, http://www.concrete.org/Publications/ACIMaterialsJournal/ACIJournalSearch.aspx?m=details&ID=11969.
10. Zhang, I., P.J.M. Monteiro, H.F. Morrison, and M. Mancio, *ACI Mater. J.* 101 (2004): pp. 273–280, http://www.concrete.org/Publications/ACIMaterialsJournal/ACIJournalSearch.aspx?m=details&ID=13360.
11. Alexander, C.L., and M.E. Orazem, *Corros. Sci.* (2019): p. 108331, https://linkinghub.elsevier.com/retrieve/pii/S0010938X19303099 (Dec. 2, 2019).

12. Alexander, C.L., and M.E. Orazem, *Corros. Sci.* 164 (2020): p. 108330, https://linkinghub.elsevier.com/retrieve/pii/S0010938X19306742.
13. Keddam, M., X.R. Nóvoa, and V. Vivier, *Corros. Sci.* 51 (2009): pp. 1795–1801, http://linkinghub.elsevier.com/retrieve/pii/S0010938X09001838 (May 26, 2014).
14. Keddam, M., X.R. Nóvoa, B. Puga, and V. Vivier, *Eur. J. Environ. Civ. Eng.* 15 (2011): pp. 1097–1103, http://www.tandfonline.com/doi/abs/10.1080/19648189.2011.9695296.
15. Tian, Z., and H. Ye, *Cem. Concr. Res.* 159 (2022): p. 106867, https://linkinghub.elsevier.com/retrieve/pii/S0008884622001594 (Jul. 13, 2022).
16. Newman, J., *J. Electrochem. Soc.* 113 (1966): p. 501, http://jes.ecsdl.org/cgi/doi/10.1149/1.2424003 (Sep. 25, 2014).
17. Newman, J., and N.P. Balsara, *Electrochemical Systems*, 4th Editio (J Wiley, 2021), https://www.wiley.com/en-us/Electrochemical+Systems%2C+4th+Edition-p-9781119514596.
18. Díaz, B., L. Freire, X.R. Nóvoa, B. Puga, and V. Vivier, *Cem. Concr. Res.* 40 (2010): pp. 1465–1470, http://linkinghub.elsevier.com/retrieve/pii/S0008884610001237.
19. Cabeza, M., P. Merino, A. Miranda, X.R. Nóvoa, and I. Sanchez, *Cem. Concr. Res.* 32 (2002): pp. 881–891, http://linkinghub.elsevier.com/retrieve/pii/S0008884602007202.
20. Díaz, B., X.R. Nóvoa, and M.C. Pérez, *Cem. Concr. Compos.* 28 (2006): pp. 237–245, http://linkinghub.elsevier.com/retrieve/pii/S0958946506000163 (May 28, 2014).
21. Andrade, C., V. Castelo, C. Alonso, and J.A. González, "The Determination of the Corrosion Rate of Steel Embedded in Concrete by the Polarization Resistance and AC Impedance Methods," in Corros. Eff. Stary Curr. Tech. Eval. Corros. Rebars Concr., ed. V. Chaker (100 Barr Harbor Drive, PO Box C700, West Conshohocken, PA 19428-2959: ASTM International, 1986), pp. 43–63, https://www.astm.org/stp18302s.html.
22. Andrade, C., F. Bolzoni, M. Cabeza, X.R. Nóvoa, and M.C. Pérez, "Measurements of Steel Corrosion in Concrete by Electrochemical Techniques: Influence of the Redox Processes in Oxide Scales," in Electrochem. Approach to Sel. Corros. Corros. Control Stud. (EFC 28). Pap. from 50th ISE Meet. Pavia, 1999, eds. P.L. Bonora, and F. Deflorian (London: European Federation of Corrosion, Institute of Materials, 2000), pp. 332–343, http://maneypublishing.com/index.php/books/efc28/.

8 FIGURE CAPTIONS

FIGURE 1. Experimental arrangement for the 2-, 3- and 4-electrode measurements performed.

FIGURE 2. Typical EIS plot obtained at high frequency for resistivity determinations in two-electrode flat condenser configuration, as shown on the left side of Fig. 1..

FIGURE 3. Typical EIS plots for resistivity measurements under Wenner-type configuration (in a 2-electrode measurement) as a function of drying time.

FIGURE 4. Comparison of resistivities determined by the reference technique (graphite electrodes placed at opposed sides of the cube) and the Wenner-type arrangement with different a spacing. A) For 1 cm distance to the embedded metallic wire. B) For 3 cm distance to the embedded wire. The error bars correspond to the standard deviations of the measurements performed on the three nominally identical specimens. The inserts correspond to enlarged views, as indicated.

FIGURE 5. Nyquist impedance plot showing the typical passive behavior of the embedded wire. The impedance was obtained in the 3-electrode configuration at the open circuit potential (-175 mV vs. SCE).

FIGURE 6. Nyquist impedance plot showing the typical active behavior of the embedded wire. The impedance was obtained in the 3-electrode configuration at the open circuit potential (-637 mV vs. SCE).

FIGURE 7. Example of a Wenner-type four-point polarization resistance measurement for three different embedded wire depths: 1, 2, and 3 cm.

FIGURE 8. Representation of the apparent polarization resistance, R_p, normalized to the resistivity, ρ, as a function of the actual polarization resistance, R_p^0, also normalized to ρ. The different values of the three parameters were obtained by sample drying as indicated.

FIGURE 9. Current distribution for (a) high frequency (1 kHz) and (b) low frequency (0.1 Hz). The more intense current gradients are represented. Parameters: ρ =1500 Ω cm, a = 2 cm, d = 1 cm, R_p= 10^5 Ω cm^2, C_{dl}= 2 μF cm^{-2}.

FIGURE 10. EIS plots obtained from the simulation process (a) two-electrode set-up and (b) four-electrode arrangement. Parameters: ρ = 1500 Ω cm, a = 2 cm, d = 0.1 cm, R_p= 10^5 Ω cm^2, C_{dl}= 2 μF cm^{-2}

FIGURE 11. Dependence of the real part of the impedance measured with the two-electrode arrangement at 1 kHz on the distance to the embedded rebar for different cement paste resistivity (in Ω cm).

9 TABLES

Table 1. A typical range of the resistivity values obtained for the blank system in the different drying conditions tested.

Condition	**ρ, kΩ cm**
Damp	1.87
1 day drying	2.77
3 days drying	3.73
1 week drying	5.51
1 more week oven drying (50 °C)	12.99

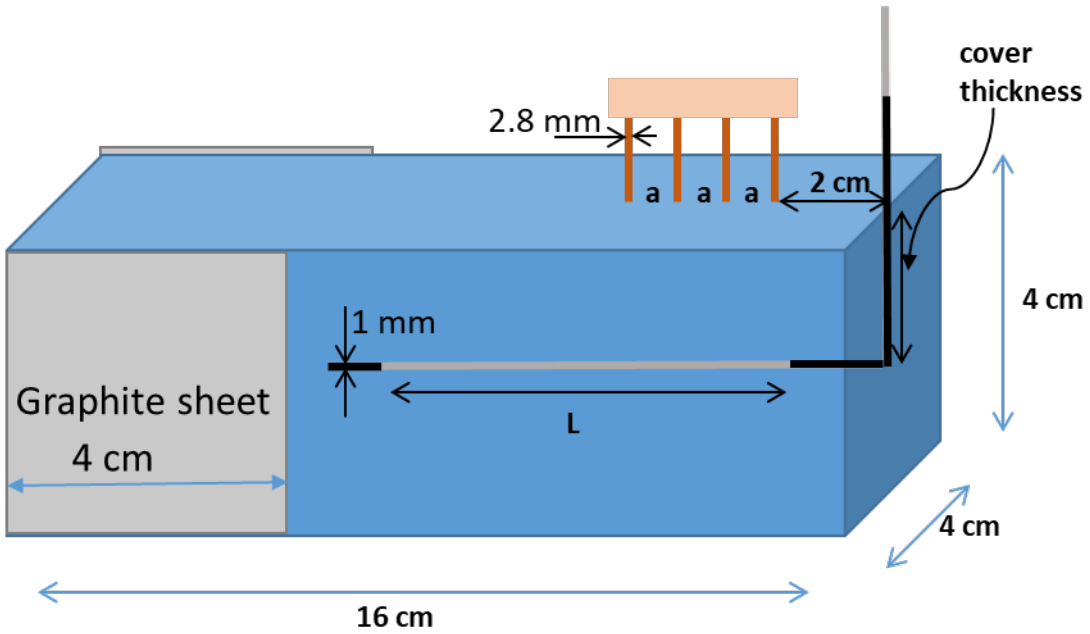

FIGURE 1. Experimental arrangement for the 2-, 3- and 4-electrode measurements performed.

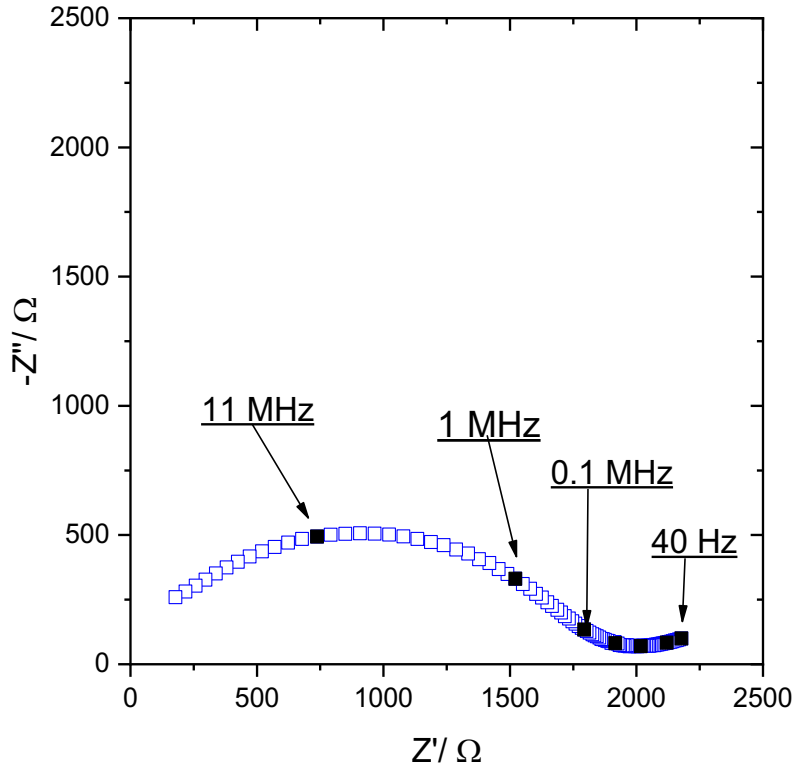

FIGURE 2. Typical EIS plot obtained at high frequency for resistivity determinations in two-electrode flat condenser configuration, as shown on the left side of Fig. 1.

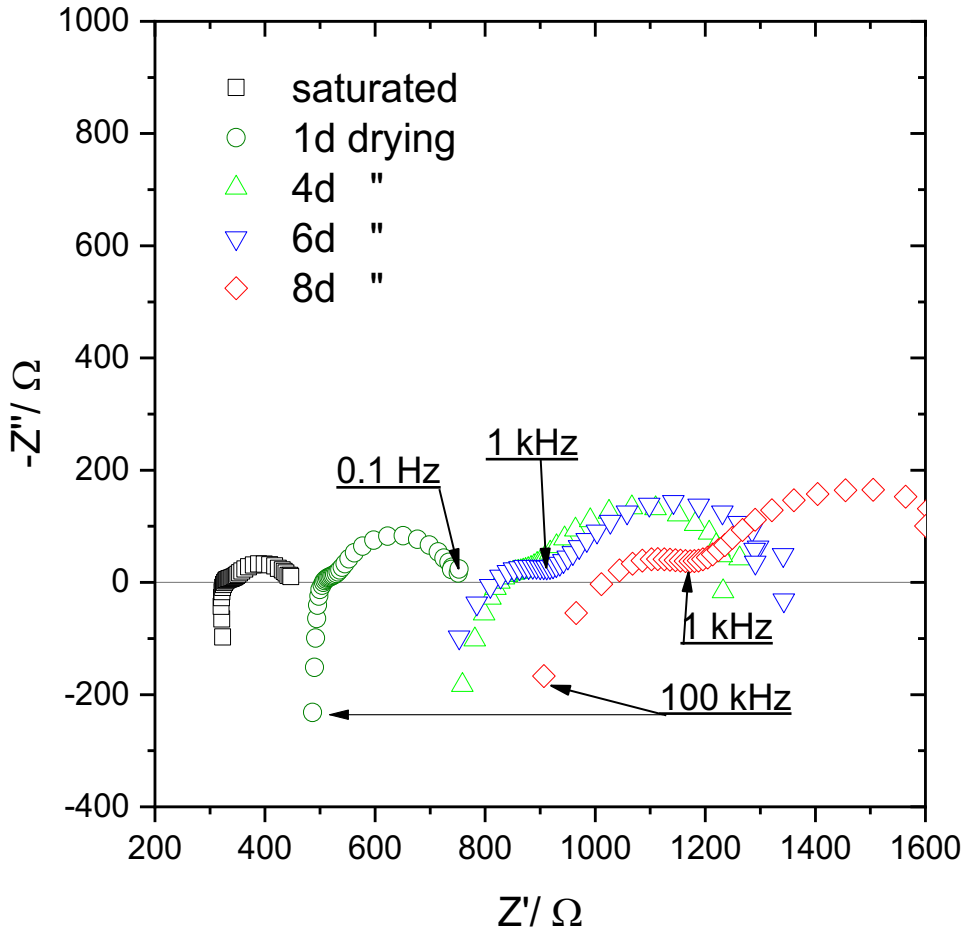

FIGURE 3. Typical EIS plots for resistivity measurements under Wenner-type configuration (in a 2-electrode measurement) as a function of drying time.

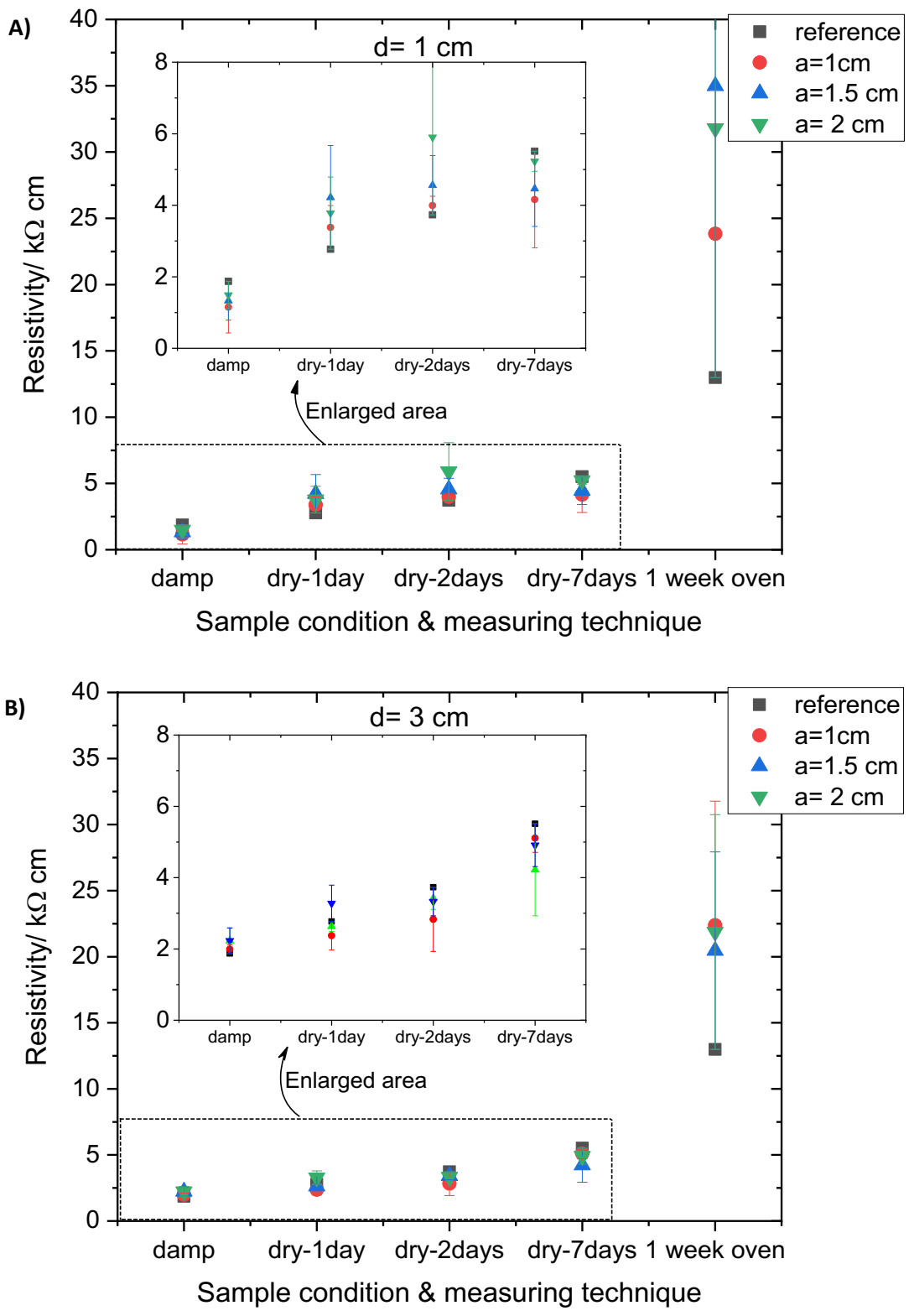

FIGURE 4. Comparison of resistivities determined by the reference technique (graphite electrodes placed at opposed sides of the cube) and the Wenner-type arrangement with different a spacing. A) For 1 cm distance to the embedded metallic wire. B) For 3 cm distance to the embedded wire. The error bars correspond to the standard deviations of the measurements performed on the three nominally identical specimens. The inserts correspond to enlarged views, as indicated.

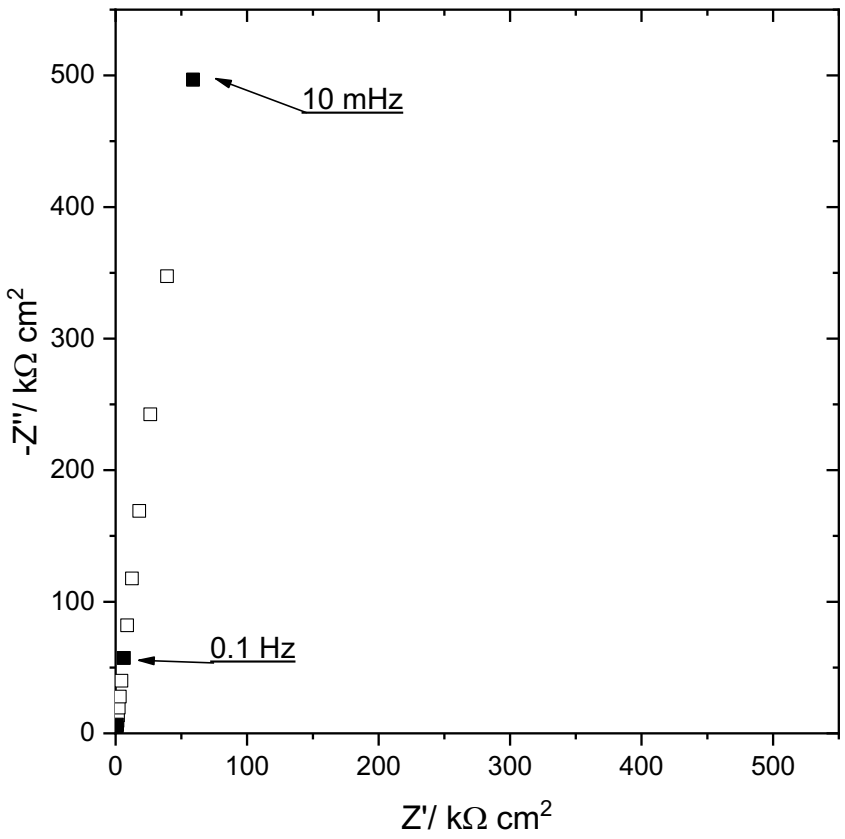

FIGURE 5. Nyquist impedance plot showing the typical passive behavior of the embedded wire. The impedance was obtained in the 3-electrode configuration at the open circuit potential (-175 mV vs. SCE).

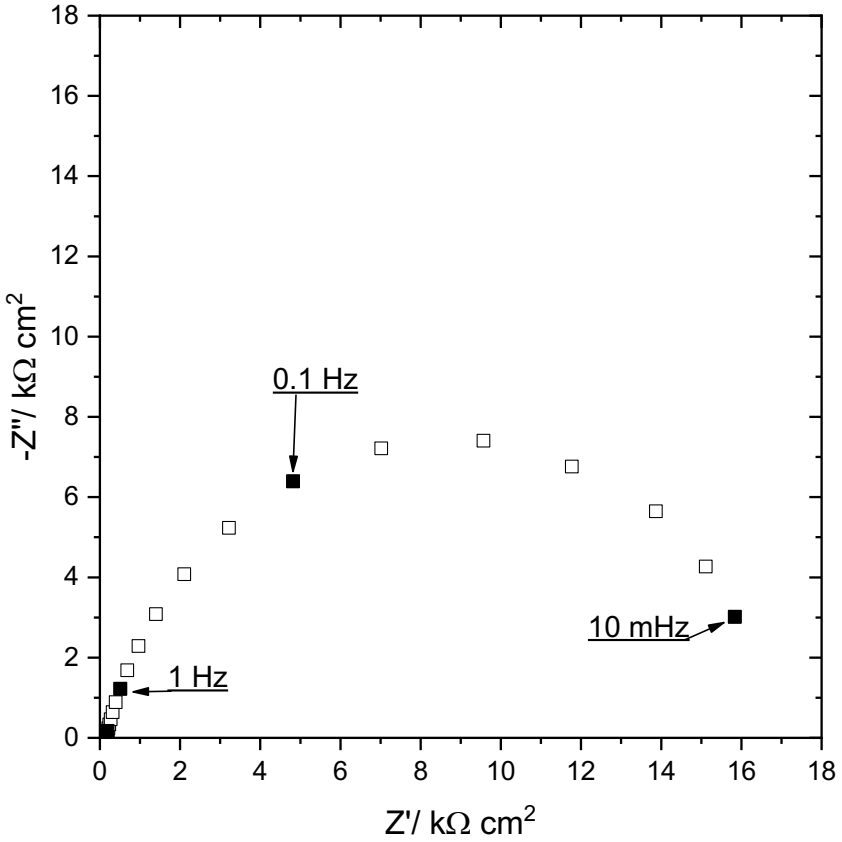

FIGURE 6. Nyquist impedance plot showing the typical active behavior of the embedded wire. The impedance was obtained in the 3-electrode configuration at the open circuit potential (-637 mV vs. SCE).

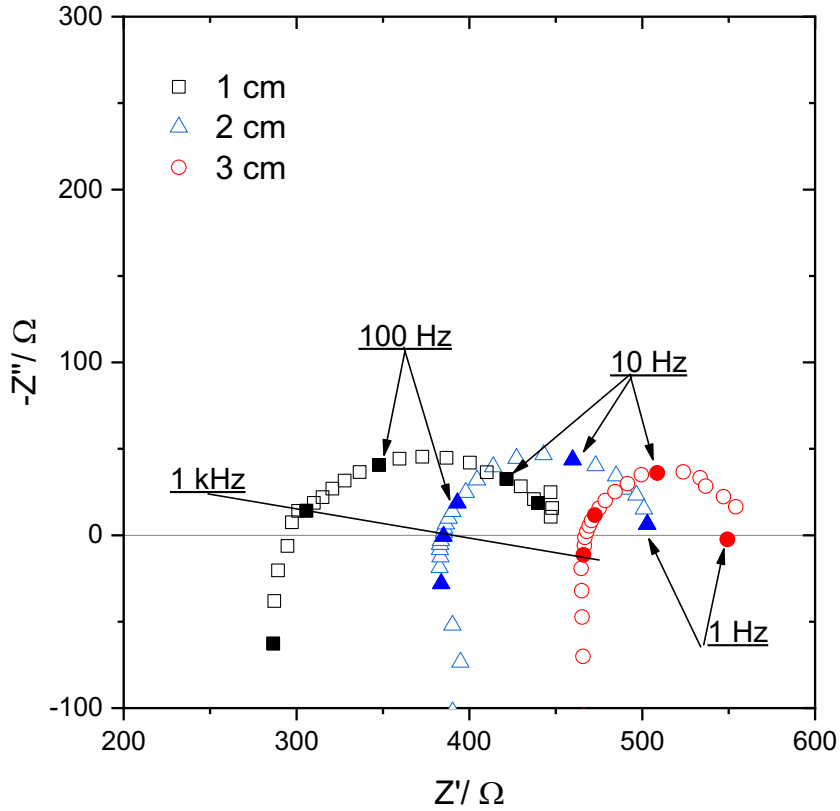

FIGURE 7. Example of a Wenner-type four-point polarization resistance measurement for three different embedded wire depths: 1, 2, and 3 cm.

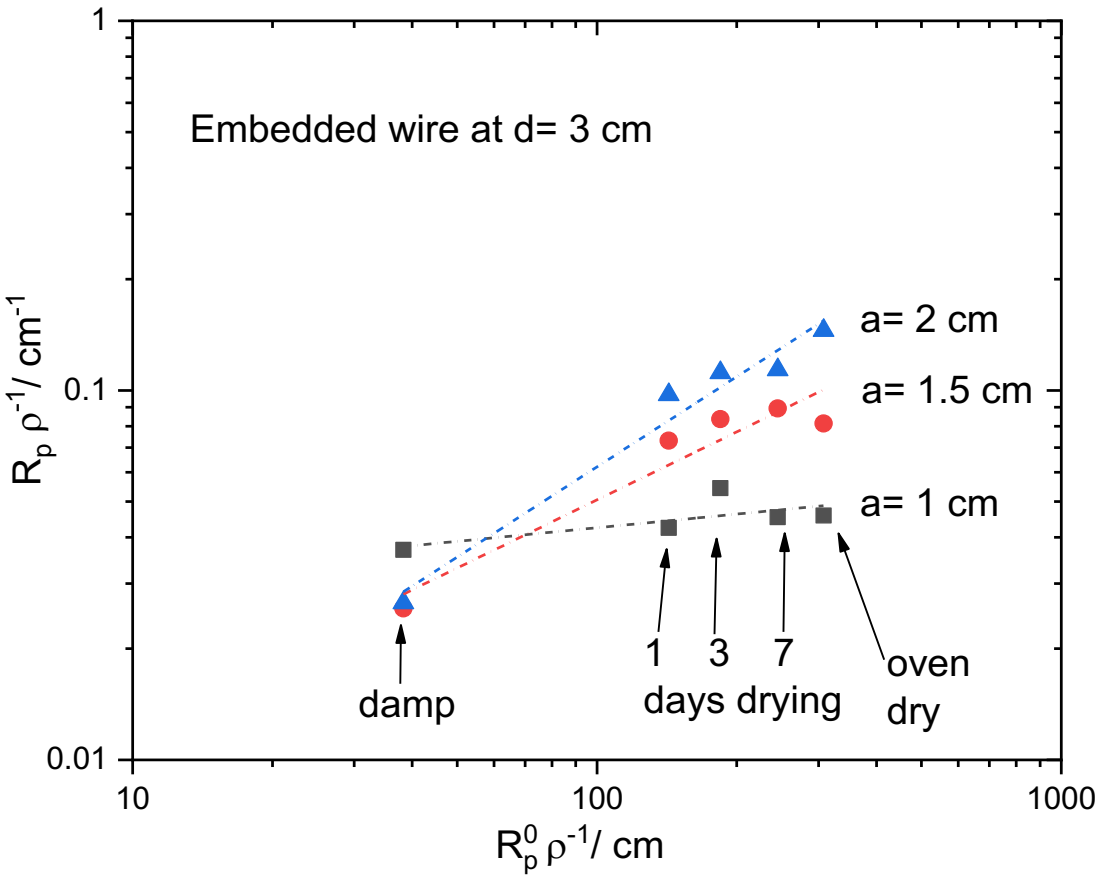

FIGURE 8. Representation of the apparent polarization resistance, R_p, normalized to the resistivity, ρ, as a function of the actual polarization resistance, R_p^0, also normalized to ρ. The different values of the three parameters were obtained by sample drying as indicated.

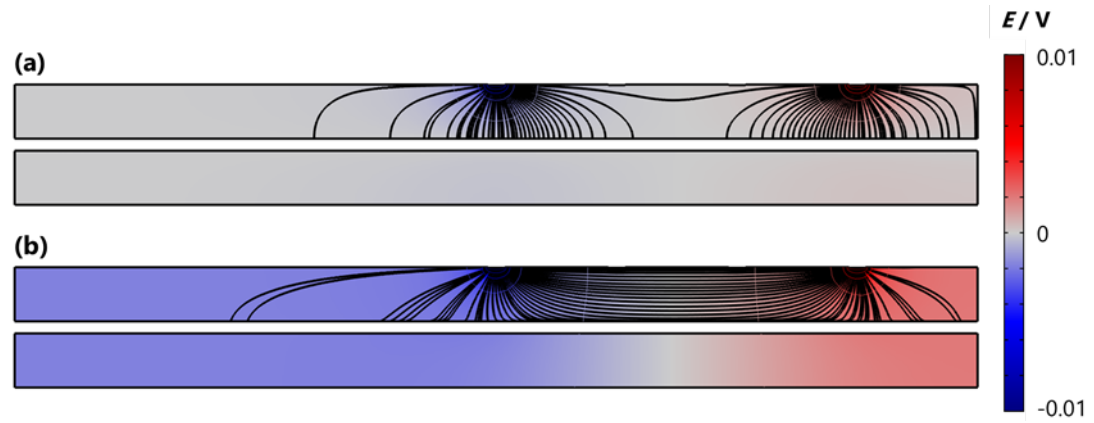

FIGURE 9. Current distribution for (a) high frequency (1 kHz) and (b) low frequency (0.1 Hz). The more intense current gradients are represented. Parameters: ρ =1500 Ω cm, a = 2 cm, d = 1 cm, R_p= 10^5 Ω cm^2, C_{dl}= 2 μF cm^{-2}.

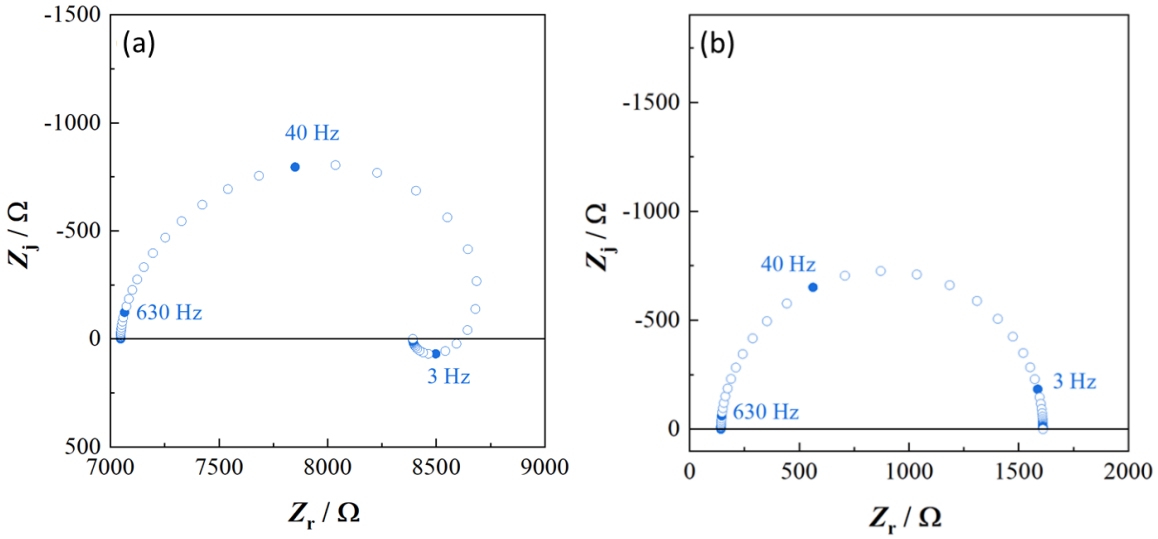

FIGURE 10. EIS plots obtained from the simulation process (a) two-electrode set-up and (b) four-electrode arrangement. Parameters: ρ = 1500 Ω cm, a = 2 cm, d = 0.1 cm, R_p= 10^5 Ω cm^2, C_{dl}= 2 μF cm^{-2}.

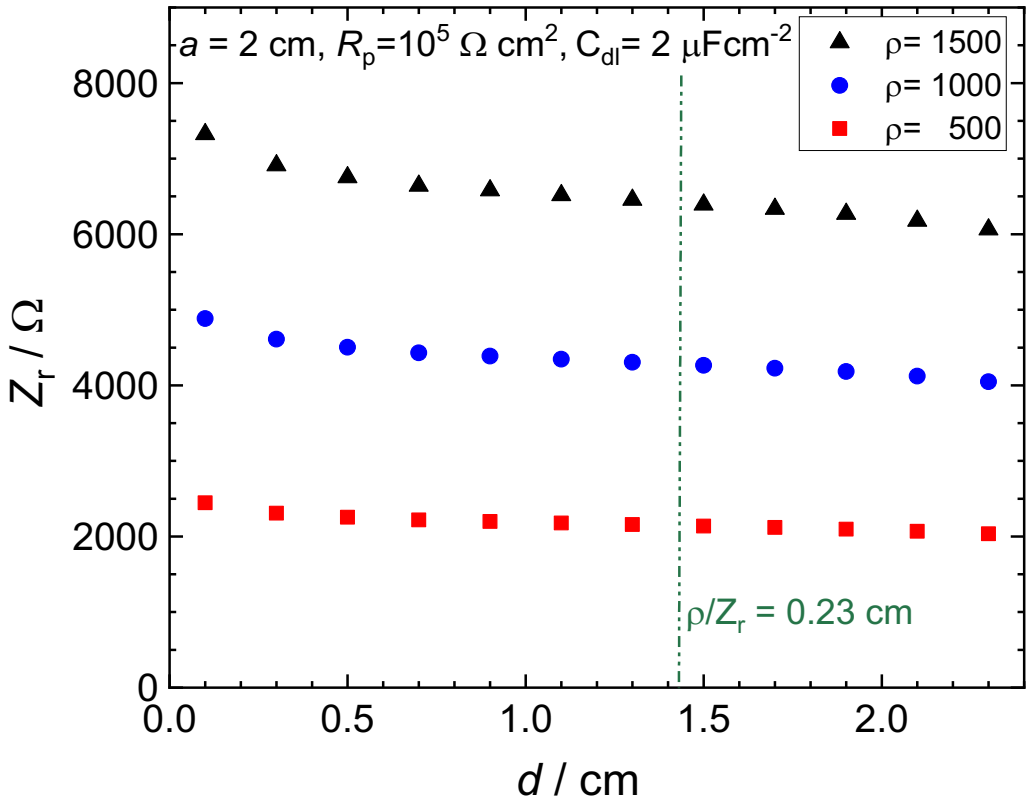

FIGURE 11. Dependence of the real part of the impedance measured with the two-electrode arrangement at 1 kHz on the distance to the embedded rebar for different cement paste resistivity (in Ω cm).